Toward high-fidelity imaging: Dynamic matching FWI and its applications

Yi Huang[1], Jian Mao[2], James Sheng[1], Mike Perz[3], Yang He[1], Feng Hao[1], Faqi Liu[1], Bin Wang[1], Seet Li Yong[1], Daniel Chaikin[1], Adriana Citlali Ramirez[4], Matt Hart[4], and Henrik Roende[1]

https://doi.org/10.1190/tle42020124.1

Abstract

Full-waveform inversion (FWI) is firmly established within our industry as a powerful velocity model building tool. FWI carries significant theoretical advantages over conventional velocity model building methods such as refraction and reflection tomography. Specifically, by solving a nonlinear inverse problem through the wave equation, FWI is able to recover a broadband velocity model containing both high and low spatial wavenumbers, thus extending the approximation of residual moveout correction inherent in traditional velocity model building approaches. Moreover, FWI is capable of inverting information from the entire wavefield (i.e., early arrivals, reflections, refractions, and multiple energy) rather than from a subset as in conventional approaches (i.e., first break and primary reflections), thereby availing itself of more information to better constrain its model estimate. However, these theoretical benefits cannot be realized easily in practice because various complexities of real seismic data often conspire to violate algorithmic assumptions, leading to unsatisfactory results. Dynamic matching FWI (DMFWI) is a newly developed algorithm that solves an inversion problem that maximizes the cross correlation of two dynamically matched data sets — one recorded and the other synthetic. Dynamic matching of the two data sets de-emphasizes the amplitude impact, which allows the algorithm to focus on minimizing their kinematic differences rather than amplitude in the data-fitting process. The multichannel correlation makes the algorithm robust for data with low signal-to-noise ratio. Applications of DMFWI across different types of acquisition and geologic settings demonstrate that this novel FWI approach can resolve complex velocity errors and provide high-quality migrated images that exhibit a high degree of geologic plausibility. Additionally, reflectivity images can be obtained in a straightforward manner as natural byproducts through computation of the directional derivative of the inverted FWI velocity models.

Introduction

As seismic acquisition methods continue to evolve, so does the efficacy of full-waveform inversion (FWI). With the industry's shift from narrow-azimuth (NAZ) streamers to wide-azimuth (WAZ) streamers, and most recently to ocean-bottom nodes (OBNs), associated acquisition advancements have enabled the capture of wider azimuth, longer offset information as well as richer frequency content. These improvements have enabled the FWI algorithm to produce model estimates of increasingly high quality, to the point where FWI has become a standard tool for high-resolution imaging in complex geologic settings. Examples of successful FWI-based mitigation of complex velocity errors abound in the literature and include cases of resolving velocity details in gas clouds, channel features, and volcanic features, as well as updating salt geometry (Mao et al., 2016; Michell et al., 2017; Shen et al., 2017; Huang et al., 2019; Wang et al., 2019).

From an inverse theory perspective, FWI can be classified as a nonlinear inversion algorithm operating in the unmigrated domain — this in notable contrast to conventional reflection tomography, which operates in the migrated images domain. Conventional FWI minimizes an L2-norm objective function defined as the sum-squared difference between input and synthetic data. This objective function can lead to unsatisfactory results on data that do not conform to the restrictive assumptions inherent in the FWI theory. The challenges for this L2-based algorithm can be summarized as follows: (1) the resulting objective function is quite sensitive to errors in the initial model; i.e., cycle skipping can lead to convergence to a local minima; (2) the direct difference of the two data sets (recorded versus synthesized) is biased by large amplitude events; and (3) the presence of strong noise in the data can have a detrimental impact, causing the inversion to diverge.

To improve the robustness of FWI, many alternative FWI formulations have been proposed. Some of these approaches are based on minimizing traveltime mismatch between input and synthetic events (Jiao et al., 2015; Y. Luo et al., 2016; Warner and Guasch, 2016; Zhang et al., 2018), while others minimize phase mismatch (J. Luo et al., 2016; Maharramov et al., 2017; Mao et al., 2019; Sheng et al., 2020). In the present approach, we exploit a fundamental characteristic of the seismic waveforms observed on both the real and synthetic data sets, namely that they tend to have similar patterns when localized in time and space. Accordingly, we seek to explicitly *maximize* local waveform similarity through use of an alternate objective function that maximizes the correlation of two dynamically matched data sets: the recorded and synthetic ones (Mao et al., 2020).

In the rest of this paper, we first briefly describe the theory of the algorithm. Then, we use different data sets to demonstrate its effectiveness. Our experience shows that dynamic matching FWI (DMFWI) carries remarkable robustness with respect to input data imperfections. The successful examples shown in the paper illustrate that DMFWI is suitable for data across different types of acquisition geometries (NAZ and WAZ towed streamer and OBN), different environments (shallow water, deep water, and land), and in various geologic settings (volcanic, salt, etc.).

---

[1]TGS, Houston, Texas, USA. E-mail: yi.huang@tgs.com; james.sheng@tgs.com; yang.he@tgs.com; feng.hao@tgs.com; faqi.liu@tgs.com; bin.wang@tgs.com; seetli.yong@tgs.com; dan.chaikin@tgs.com; henrik.roende@tgs.com.
[2]Formerly TGS; presently Schlumberger, Houston, Texas, USA. E-mail: jmao6@slb.com.
[3]Formerly TGS; presently EOG Resources, Houston, Texas, USA. E-mail: michael_perz@eogresources.com.
[4]TGS, Woking, UK. E-mail: adriana.citlali.ramirez@tgs.com; matt.hart@tgs.com.

DMFWI cost function

A key cog in the DMFWI engine is a technique known as local cross correlation, a method that is good for measuring similarity and phase differences between two waveforms. While local cross correlation based on time windowing alone can be used in principle for measuring both characteristics, experience shows that the approach can be sensitive to noise in the data, especially coherent noise and/or noise bursts (e.g., blend noise, swell noise, or turning noise). By contrast, use of a multidimensional window (i.e., both time and space) allows us to take full advantage of the lateral coherence of the signal, thereby improving the reliability of the overall matching process and ultimately guiding the velocity updates to match synthetic with real signal. Specifically, DMFWI uses an objective function based on multidimensional local cross correlation of the form:

$$E_{mc} = \int_{x_s}\int_{x_r}\int_0^T c_m\left(x_s,x_r,t\right)dt\,dx_r\,dx_s, \tag{1}$$

where $c_m\left(x_s,x_r,t\right) = \int_{-x_0}^{x_0}\int_{-\tau_0}^{\tau_0} w\left(x,\tau\right)\bar{d}\left(x_s,x_r+x,t+\tau\right)\bar{u}\left(x_s,x_r+x,t+\tau\right)d\tau\,dx$ is a multidimensional local cross correlation in which $w(x,\tau)$ is a window function of half-length τ_0, x_0 in the time and space domain, respectively (we assume a 2D case for simplicity in exposition), $\bar{d}(x_s,x_r+x,t+\tau)$ and $\bar{u}(x_s,x_r+x,t+\tau)$ represent the dynamically normalized versions of the input data and synthetic data in local windows, and subscripts s and r denote source and receiver indices, respectively. This local cross correlation is insensitive to local amplitude differences between the measured and synthetic waveforms, and it benefits from additional ruggedizing constraints applied in both the data and model domains as described by Sheng et al. (2020). Frequency-dependent changes in waveform are readily accommodated by allowing the temporal and spatial window sizes to vary with frequency, a modification that is naturally incorporated within a multiscale approach (i.e., where we step from low frequencies to higher ones via multiple FWI passes). Experience shows that the DMFWI approach gives reliable inversion results even in the presence of strong noise, including cases where DMFWI is run on raw field data.

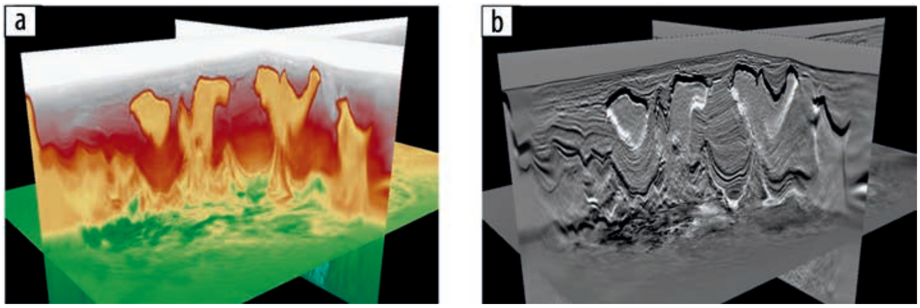

Figure 1. Deepwater Gulf of Mexico dual WAZ example. (a) Final velocity model after DMFWI. (b) FWI image corresponding to (a).

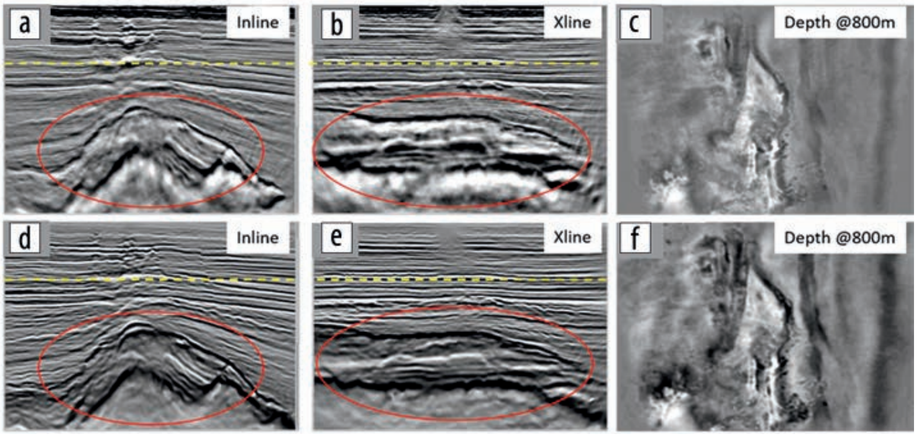

Figure 2. Comparison of FWI imaging and conventional migration on a West of Shetland OBN data set. (a), (b), and (c) Final 80 Hz Kirchhoff migration results along inline, crossline, and depth slice, respectively. (d), (e), and (f) Corresponding 50 Hz FWI imaging results. Yellow dashed line in vertical sections indicates the 800 m depth level shown in the depth slices in (c) and (d).

DMFWI and FWI imaging

DMFWI's value in steering FWI toward a high-quality result may be further amplified considering the new application known as FWI imaging (Kalinicheva et al., 2020; Zhang et al., 2020; He et al., 2021; Wang et al., 2021). FWI imaging is essentially the process of converting the final FWI-estimated property field to a reflectivity volume. Mathematically, this conversion is achieved in a straightforward manner by computing the normal derivative at all points in the property volume. Figure 1a shows a final velocity model after DMFWI from a dual WAZ survey acquired in deepwater Gulf of Mexico, and Figure 1b shows the corresponding FWI image obtained after applying the aforementioned differentiation. The latter image bears an obvious resemblance to a familiar "reflectivity-based" migrated section.

The intrinsic similarity between FWI imaging and conventional migration is further explored in Figure 2 where we display both final migrated sections (Figures 2a–2c) and FWI images (Figures 2d–2f) from a shallow-water OBN survey acquired over the Clair Field, West of Shetland, UK. This example is discussed in more detail in the case history section to follow. For now, we wish to emphasize both the general similarity between migrated and FWI image sections as well as intriguing differences, with the FWI image exhibiting improved continuity and focusing over its migrated counterpart in many places (e.g., red ellipses) — this despite the discrepancy in maximum frequency used in creating the two results (80 Hz Kirchhoff migration versus 40 Hz FWI image). Additional

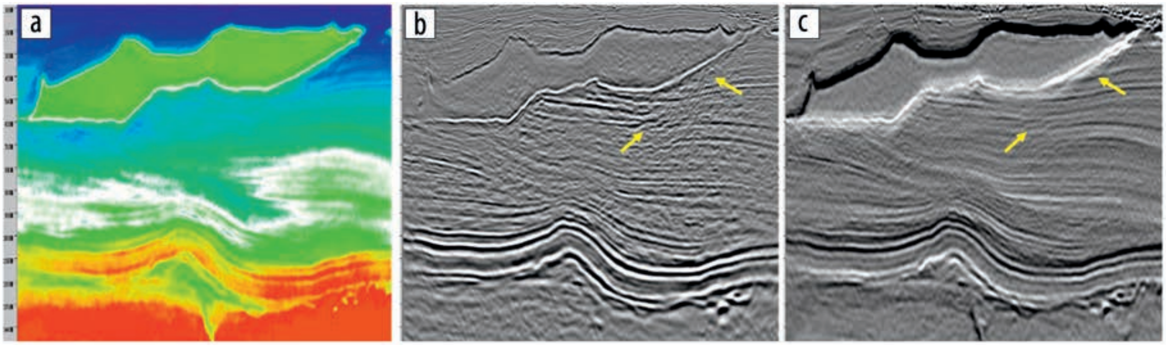

Figure 3. Comparison of FWI imaging and LS-RTM on a sparse, ultra-long-offset OBN data set from the Gulf of Mexico. (a) Final model after DMFWI. (b) Migrated inline after LS-RTM using DMFWI-updated model. (c) Same inline as (b) but after FWI imaging.

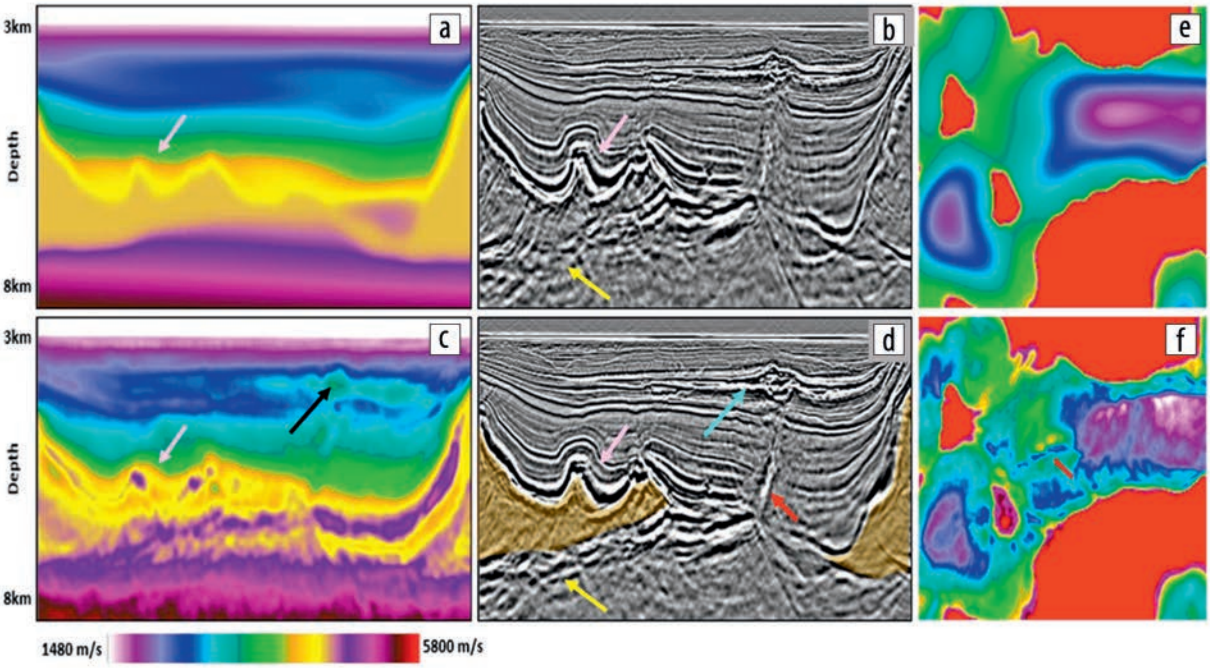

Figure 4. Campos NAZ velocity models and migrated images before and after DMFWI. (a) Initial model. (b) Migrated image associated with initial model. (c) Final model after DMFWI. (d) Migrated image associated with final model, with salt interpretation shown in yellow fill. (e) 6 km depth slice through initial model. (f) 6 km depth slice through the final model in which dike features are resolved. Arrows highlight key changes.

evidence in support of FWI imaging producing excellent images is shown in Figure 3, an example drawn from a deepwater Gulf of Mexico OBN survey also featured in the case history section of this paper. Note that this example compares an FWI image to least-squares reverse time migration (LS-RTM), the latter being an expensive algorithm known to improve image resolution and reduce imaging artifacts that may be present in conventional reverse time migrations (RTMs). Yellow arrows show where the FWI image has captured small fault features and has improved termination of the events against the base salt canopy. It is obvious that DMFWI's robustness will play an important role in producing the high-quality models required for FWI imaging as this exciting new approach gains traction in our industry.

DMFWI field examples

DMFWI has been applied successfully to many challenging data sets with different acquisition geometries, imparting unprecedented detail to models and providing high-fidelity image improvements in complex geologic settings that have proved challenging with pre-existing model building methods. While the examples featured here are offshore, recent experience with DMFWI on land data suggests that the algorithm can also produce excellent results in onshore settings, where the robust objective function provides an important safeguard against the strong noise typically observed on land records.

NAZ data from deepwater offshore Brazil. Our first example is a NAZ streamer data set from the Campos Basin, offshore Brazil, which was recorded with 10 km cables at 100 m separation. Campos Basin is characterized by thick Aptian salt over an oil-rich presalt, directly overlain by Albian carbonates with near-salt velocities and then by younger slower units. One imaging challenge is the presence of volcanic dikes and sills. The volcanic intervals have variable velocities but are significantly faster than the surrounding sediments. These volcanics are relatively thin, varying from hundreds of meters down to a few meters, resulting in small-scale velocity heterogeneities that are challenging to resolve but crucial for imaging key prospective areas. Experience has shown that conventional workflows based on tomography and/or human interpretation cannot provide the required degree of accuracy, which makes this a great candidate for FWI.

DMFWI succeeded in delineating the volcanic velocities and improved the overall image. The initial model input into FWI is shown in Figure 4a with the corresponding migrated image shown in Figure 4b. The DMFWI-updated velocity model is shown in Figure 4c with the corresponding revised migrated image in Figure 4d. There are several key improvements:

- higher volcanic velocities are inserted (black arrow, Figure 4c) along the thin horizontal volcanic sill (cyan arrow, Figure 4d);
- velocities are refined within Albian-age carbonate layers lying directly atop the salt (pink arrows, Figures 4a–4d);
- within the Albian carbonates and under the volcanic sill, a thin volcanic dike, previously blurred, is now focused (red arrow in Figure 4d); moreover, the trend of this structure is captured in the velocity model (Figure 4f, red arrow);
- salt velocity (initially a constant velocity of 4500 m/s) is refined; and
- the imaging of presalt structure is improved (see especially yellow arrow in Figure 4d and compare to corresponding arrow in Figure 4b).

These improvements were realized despite limited low frequencies in the data set, with reliable signal unavailable below 4 Hz.

Dense, shallow-water OBN data from West of Shetland, UK. Our second example is a high-density marine (OBN) survey acquired by BP in 2017 over the Clair Field with a source sampling of 25 × 25 m and a receiver sampling of 50 × 100 m. The Clair Field is located approximately 75 km west of the Shetland Islands in shallow water (roughly 140 m depth). Figures 5a, 5b, and 5c show an inline, crossline, and 800 m depth slice, respectively, extracted from the initial model, while Figures 5d–5f show the corresponding sections from the model obtained after running high-resolution DMFWI up to 40 Hz. A considerable amount of model sedimentary detail is resolved after DMFWI. This results in flatter and geologically plausible events on the migrated volume created using the DMFWI-updated model (Figures 5j–5l, where corresponding initial-model migrated volume is shown in Figures 5g–5i).

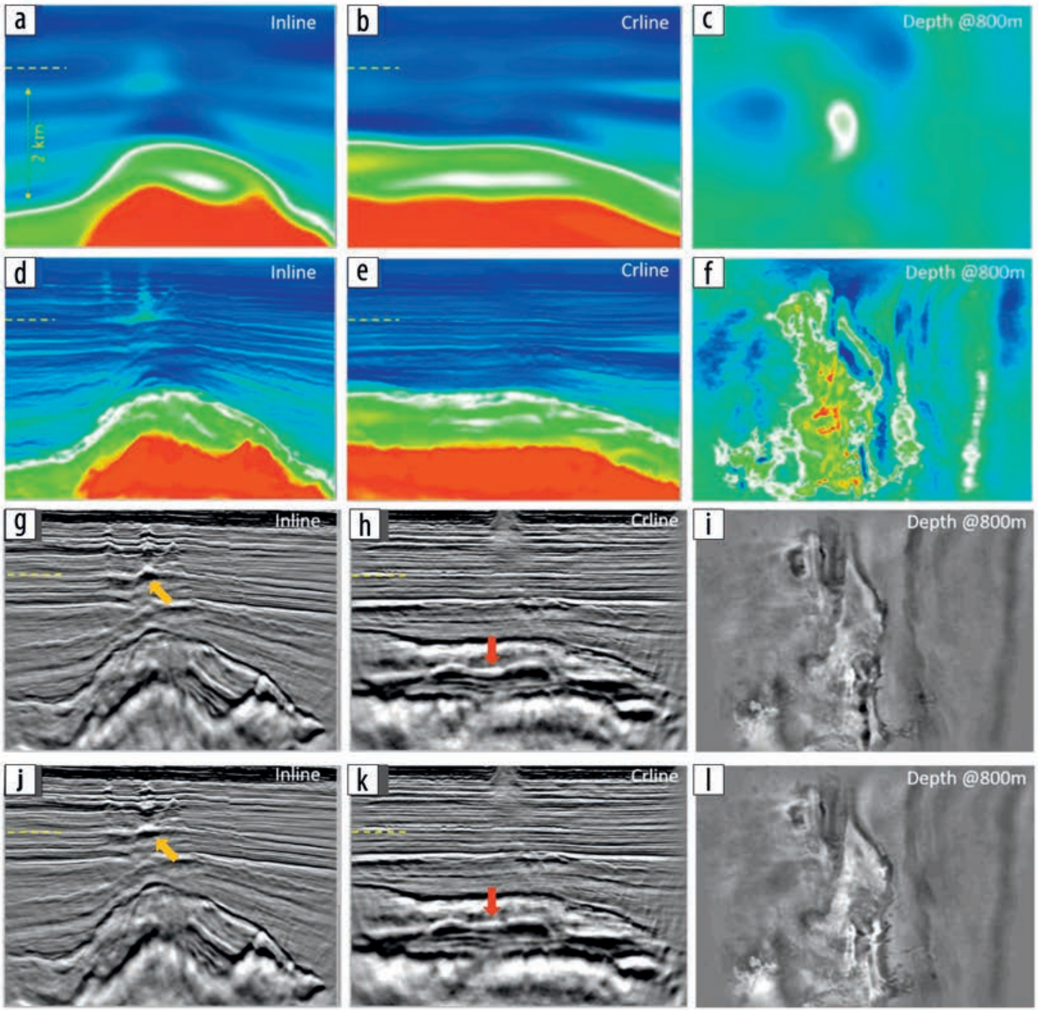

Figure 5. Clair OBN DMFWI results. (a), (b), and (c) Initial velocity model along inline, crossline, and 800 m depth slice, respectively. (d), (e), and (f) Same as (a), (b), and (c) except model is after DMFWI. (g), (h), and (i) 80 Hz Kirchhoff migration associated with initial model. (j), (k), and (l) 80 Hz Kirchhoff migration associated with final model after DMFWI. Yellow dashed lines on vertical sections indicate the 800 m depth level shown in the depth slices in (c), (f), (i), and (l).

Dense shallow-water OBN data from North Sea. Here we explore another European shallow-water OBN data set with a bathymetry averaging 110 m. The area is located approximately 350 km southeast of the Clair Field in the South Viking Graben, North Sea. Despite its geographic proximity to Clair, the geology and associated imaging issues in the present example are very different. The survey covers an area of more than 2000 km^2, with a variety of plays ranging in stratigraphy from Tertiary to Paleozoic basement. Key seismic challenges include complex overburden (shallow channels, shallow gas, and injectites — also known as v-brights) generating strong multiples and leading to poor reflector continuity, insufficient illumination of subsurface targets, and inaccurate delineation of structural faulting at the target area. Injectites are intrusive sands with high velocity and impedance contrast relative to the surrounding host rock, which are often prospective. Deriving a sufficiently accurate velocity model and proper placement of these geobodies in the migrated cubes require an abundance of azimuthal information and low-frequency signal, both of which are available in our full-azimuth OBN survey.

In 2019–2020, a regional processing effort was undertaken on this OBN data set. The workflow inverted early-arrival energy only using a maximum inline offset of 6.7 km and a maximum frequency of 5 Hz. Thus, the FWI updates were limited to the overburden (approximately the first kilometer, above the average level of the injectites), while the model of the deeper section relied purely on traditional model building based on tomography. The regional processing effort produced an acceptable low-resolution velocity model, and the resulting final image revealed good placement of the injectites, reflector continuity, and fault characterization. However, it did not realize the full potential of the densely sampled OBN in terms of resolution. Accordingly, in 2020–2021 we embarked on a new velocity model building effort using DMFWI with the ambition of achieving an interpretable model that explicitly included the injectites. Our DMFWI workflow

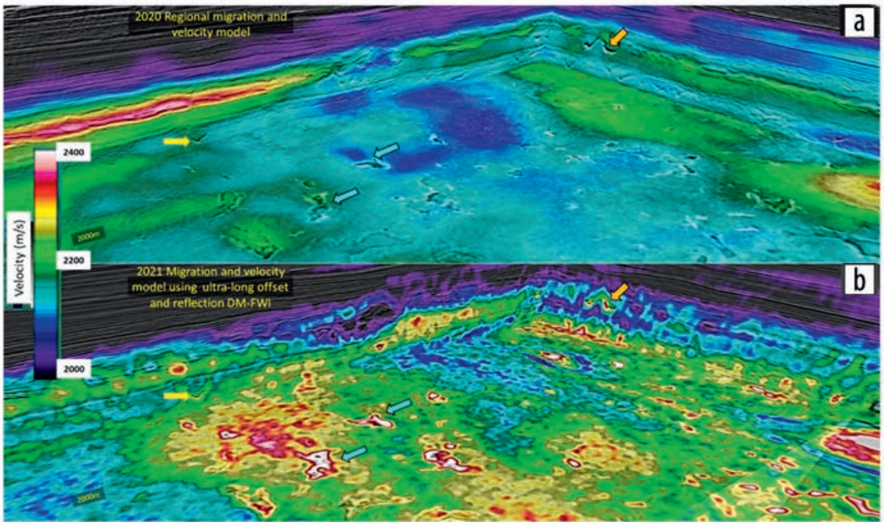

Figure 6. Chair diagram of North Sea OBN FWI-based velocity models overlain atop final migrated images. Both model building efforts included well calibration and anisotropy updates. (a) 2020 regional processing. (b) 2021 detailed processing using DMFWI.

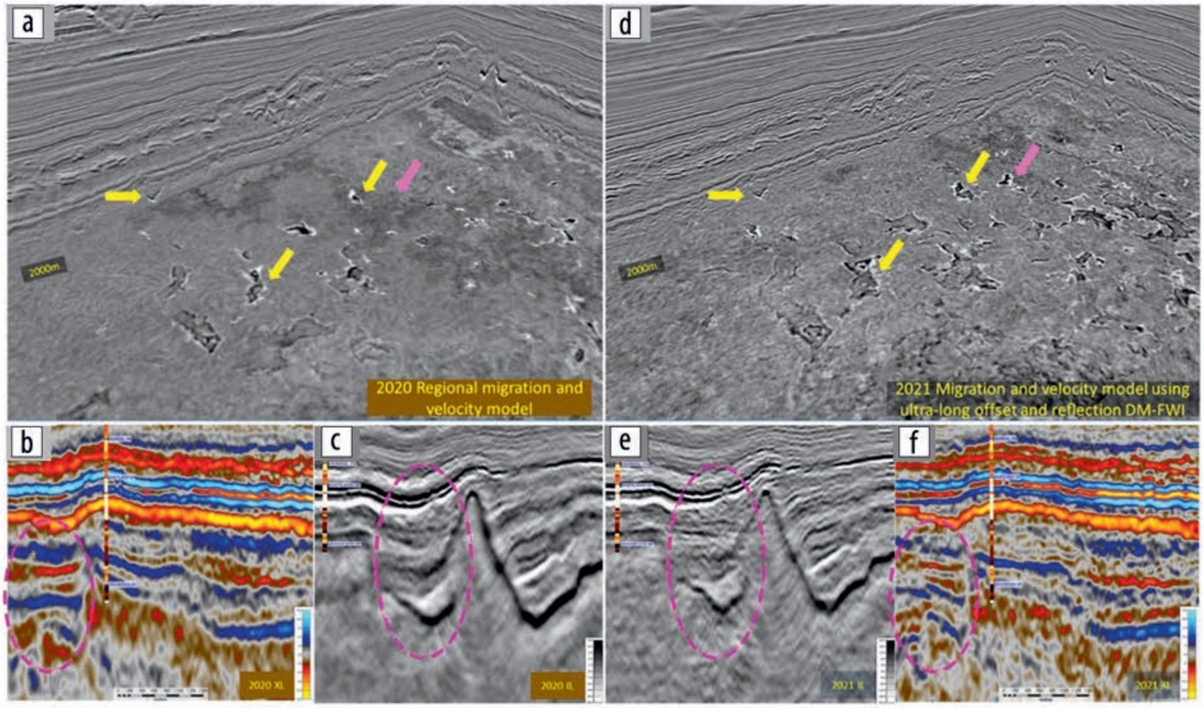

Figure 7. North Sea OBN final migrated images: (a), (b), and (c) show 2020 regional processing result in chair diagram, crossline, and inline views, respectively; (d), (e), and (f) show 2021 detailed processing result in chair diagram, inline, and crossline views, respectively.

included use of longer offsets (up to 17 km maximum inline offset) and higher frequencies (f_{max} = 12 Hz), as well as the incorporation of both early-arrival and reflection energy. In addition to DMFWI, the model building included well calibration and anisotropy updates within the FWI model building workflow, and it was refined via multiazimuth Kirchhoff tomography (six sectors) followed by another pass of well calibration and anisotropy update. Final velocity models produced by both regional (2020) and new (2021) workflows are overlain atop corresponding migrated seismic images in Figure 6. The vertical-section views of both regional (Figure 6a) and new (Figure 6b) results show an inline and crossline above 2000 m, where numerous injectites are visible (e.g., yellow arrows). Not only does the new DMFWI workflow provide improved imaging resolution compared to the regional one, it also produces a velocity model that allows direct interpretation of injectites (e.g., orange arrows). The velocity depth slice at 2000 m also crosses injectites whose contours are clearly visible in both model and migrated image in the new result (blue arrows) but not in the regional one.

Figure 7 tells a similar story but focuses on the migrated images without the distraction of the velocity overlay. Figures 7a–7c show the regional result, and Figures 7d–7f show the new 2021 result. There are obvious and dramatic improvements in the resolution of the structure, horizons, faults, and injectites throughout the new volume. Among other things, injectite imaging is much crisper and more accurate in both section and depth slices in the new result in Figure 7d compared to the regional result in Figure 7a (yellow arrows), with the pink arrows highlighting a case where an injectite is altogether absent in the regional result. The color images in Figures 7b and 7f are crosslines from regional and new results, respectively, and they highlight some very large differences. For example, some reflectors dipping in different directions in the regional data have been corrected in the new data (magenta ellipses). In addition, the inline sections in Figures 7c and 7e show a change in structure due to improved image resolution (magenta ellipses).

Beyond detection and resolution of injectite bodies, the ability to accurately discern between brine-filled (nonprospective) and hydrocarbon-filled (prospective) fluids residing inside injectite pore spaces carries obvious economic benefit. Figure 8 shows a depth slice that intersects drilled hydrocarbon-filled (left column: Figures 8a–8c) and drilled brine-filled (right column: Figures 8d–8f) injectites as shown by red ellipses. The top row (i.e., Figures 8a and 8d) shows the 2020 regional velocity model overlain by the seismic, the middle row shows the corresponding model and seismic from the new 2021 model building effort, and the lower row shows a velocity model predicted by a completely independent machine learning (ML) workflow that used the regional model, regional image, and wells in the area as input (Jansen et al., 2021). Both DMFWI-predicted (Figures 8b and 8e) and ML-predicted (Figures 8c and 8f) velocity models support field observations indicating that higher velocity is associated with nonprospective injectites and lower velocity with prospective ones. Although the DMFWI and the ML-based models have distinctly different resolution due to the nature of the algorithms used to derive them, the geologic insights they provide are largely consistent at a broad scale and hence reinforce confidence in results. By contrast, the velocity model from the 2020 regional processing (Figures 8a and 8d) does not have enough resolution to support a meaningful interpretation of fluid content.

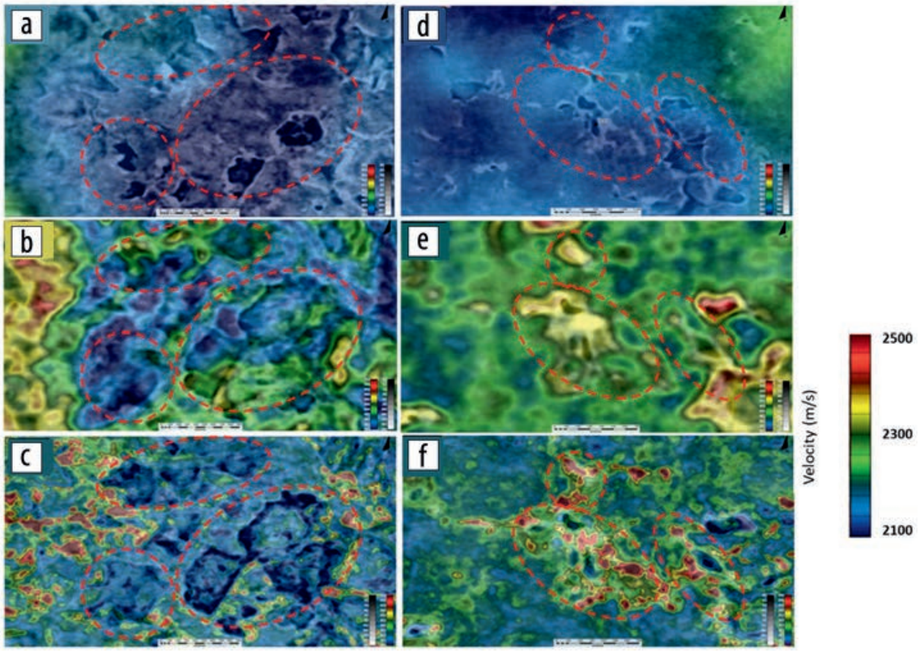

Figure 8. Utsira OBN final velocity model depth slices at approximately 1600 m: (a), (b), and (c) show models crossing prospective injectites (red ellipses) from regional processing, new model building, and ML-based prediction, respectively; (d), (e), and (f) show corresponding model results crossing nonprospective injectites. Both regional and DMFWI models are overlain by the seismic.

Ultra-long-offset sparse OBN from deepwater Gulf of Mexico. Our fourth example is from an ultra-long-offset sparse OBN survey collected in the eastern part of the Gulf of Mexico in 2019 across an area featuring massive shallow and deep structurally connected salt masses The acquisition was explicitly designed for FWI application, leading to dramatic improvements in image quality compared to traditional (non-FWI-based) imaging approaches. The nominal node spacing is 1000 × 1000 m and source spacing is 50 × 100 m. A minimum 40 km offset for each node location was acquired in order to capture diving waves down to the original Louann salt level. Detailed information about the acquisition design and the challenges in preparing the data can be found in Roende et al. (2020). The study area contains an assortment of complex structures related to salt tectonics, including large-scale salt feeders with well-developed megaflaps connecting deeper, in-situ Louann salt to salt canopies. Sharp velocity variations include slow-velocity gas chimneys, a dramatic velocity difference between

Miocene and younger sediments and adjacent salt, and, at depth, hard Mesozoic carbonates with velocities faster than salt.

Although we put a great deal of effort into refining our tilted orthorhombic legacy model, including many iterations of high-resolution tomography and intensive human salt interpretation, the legacy model still struggles to reveal accurate velocity details in this geologically complex environment. By contrast, the model obtained after DMFWI reveals a wealth of previously obscured and complex detail whose geologic plausibility is affirmed by the high quality of the corresponding migration. Figures 9a and 9b display an inline and crossline through the initial velocity model, while Figures 9c and 9d show corresponding DMFWI sections. Figure 10 shows the corresponding migrated seismic sections, which reveal stunning uplift after DMFWI. The capture and delineation of fast-velocity carbonates, including where near vertical along salt walls, provide both the biggest change to the model (red arrows, Figures 9c and 9d) and a fundamental improvement in imaging the structure of previously obscured salt stocks and associated megaflaps (pink arrow, Figure 10c). This is the main model update that led to a significant uplift in focusing the base of Louann salt (yellow arrows, Figure 10c), which confirms overall velocity integrity and accentuates presalt features (orange arrow, Figure 10d). In addition to the aforementioned improvements, there are numerous other significant changes to the model as well as obvious uplift in the associated imaging. Two other significant model enhancements are slower velocities of shallow gas chimneys and clouds (black arrows, Figure 9c) and refinements of the salt geometry and of inner-salt features, such as where two inner-salt inclusions in the input model are mostly removed (yellow

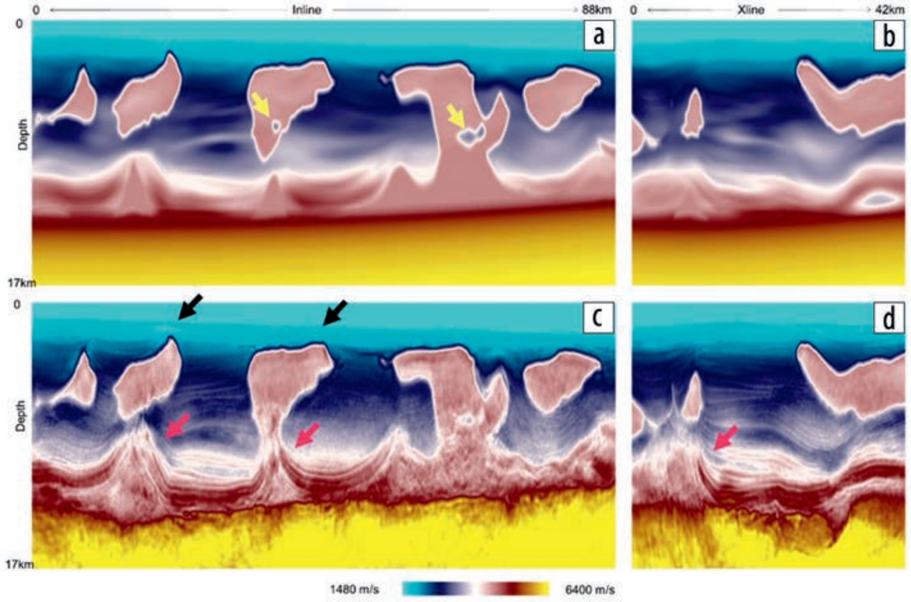

Figure 9. Amendment sparse OBN velocity models. (a) and (b) Initial model along inline and crossline directions, respectively. (c) and (d) Final model after DMFWI along inline and crossline, respectively. Arrows point to features discussed in the text.

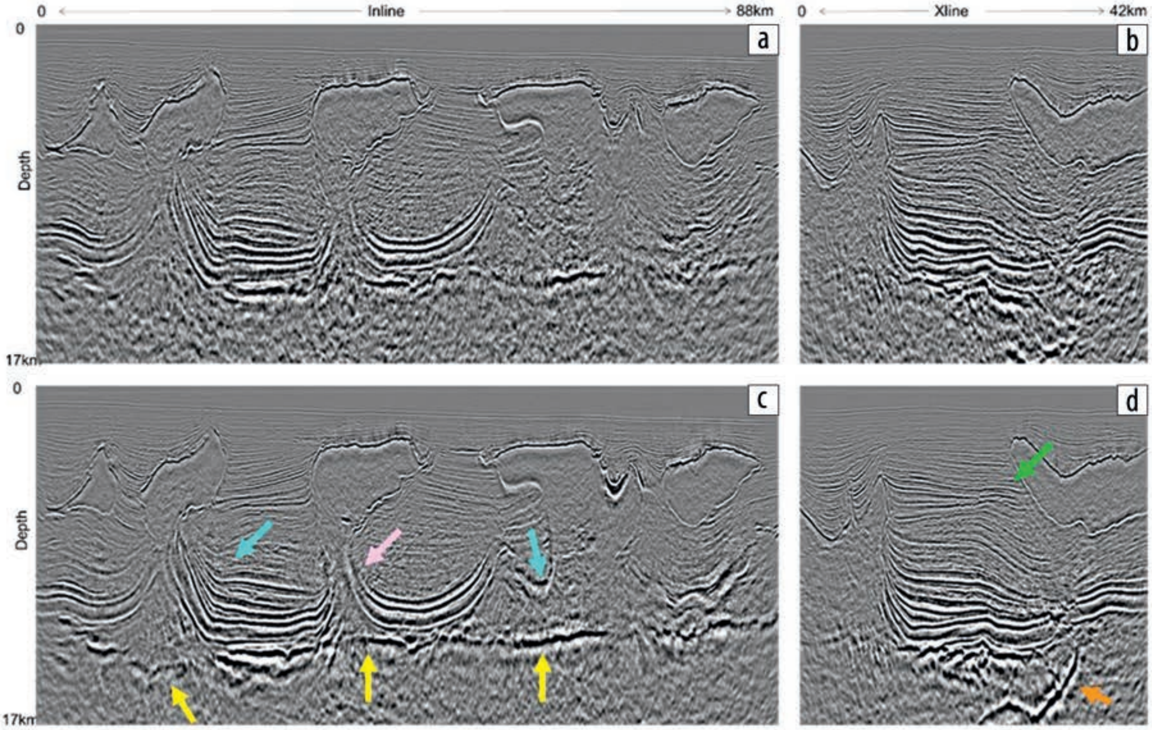

Figure 10. Gulf of Mexico sparse OBN migrated images before and after DMFWI. (a) and (b) Migrated images associated with initial model along inline and crossline directions, respectively. (c) and (d) Migrated images associated with DMFWI model along inline and crossline directions, respectively. Arrows point to imaging improvements discussed in the text.

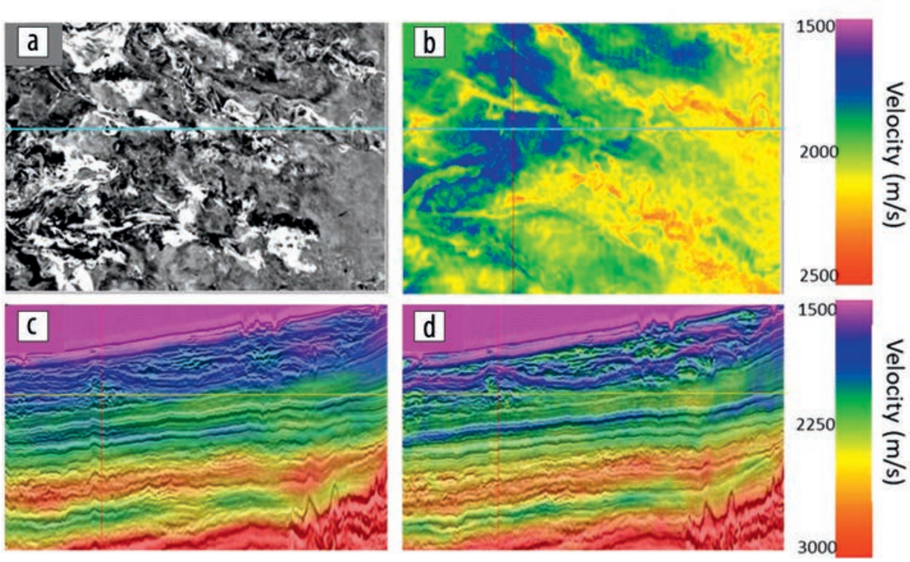

Figure 11. Gabon NAZ DMFWI example. (a) Depth slice of intermediate migration (z = 2.4 km) illustrating shallow sediment complexity. Blue horizontal line indicates approximate location of crossline shown in (c) and (d). (b) Depth slice of final velocity model after DMFWI update (z = 2.4 km). (c) Initial model overlaid atop crossline migrated using initial model. (d) Final (DMFWI-updated) model overlaid atop crossline migrated using final model.

arrows, Figure 9a). The entire subsalt model is improved, and significant detail is added, resulting in the healing of near-salt sediment breaks in the migrated image (green arrow, Figure 10d) as well as improvement in the subsalt sediment structure (cyan arrows, Figure 10c).

NAZ data from deepwater offshore Gabon. Our final example is a NAZ streamer survey located in deepwater offshore Gabon acquired with a 7 km cable length at 100 m separation. Due to the water depth and short cable length, there was limited coverage of diving wave energy in the survey area.

The shallow sediments beneath the rugose seabed form a complex series of multilevel channels and deltaic fan deposits as can be seen from the intermediate migration depth slice at z = 2400 m shown in Figure 11a. These shallow structures are composed of highly variable sediments with low-velocity shales/muds and higher-velocity sand lenses. Undulations visible in the underlying Oligocene and Cretaceous sediments in the legacy migration (Figure 11c) are presumably due to imperfections in estimating the large velocity variations present within these shallow structures.

The initial velocity model was derived from several passes of image-guided tomography. DMFWI was then used to refine that model to resolve the strong velocity heterogeneity within the sediments in the vicinity of the shallow channel formations. Figure 11b shows a depth slice of the model after DMFWI from the same level (z = 2400 m) as the intermediate migration shown in Figure 11a. While this shallow model contains a small amount of acquisition footprint (removed in subsequent model refinement), it also reveals exquisite detail in the shallow geology, including obvious channel features whose patterns are generally consistent with the migrated slice in Figure 11a. Migration using this DMFWI-updated model produces the image shown in Figure 11d. By comparing this final migrated image to its initial-model counterpart in Figure 11c, we see that DMFWI has done an excellent job in removing undulations in the underlying Oligocene and Cretaceous sediments.

Conclusions

This paper describes DMFWI, a novel algorithm of FWI whose effectiveness has been demonstrated with its successful application to many data sets across different geologic settings and acquisition configurations. The algorithm's ability to dynamically match observed and predicted data provides it with remarkable robustness with respect to noise and relative insensitivity to elastic effects that are not properly modeled by an acoustic kernel. Additional constraints posed in both data and model domains also play a large role in forcing its convergence to a geologically plausible model. The algorithmic advantages directly benefit the FWI imaging process, resulting in high-resolution reflectivity images that extend FWI's applicability beyond velocity model updating into the realm of direct inversion for structural images.

Acknowledgments

We thank TGS and partner WesternGeco for permission to show the Amendment sparse OBN data set, as well as BP and its partners (Shell, Chevron, and Harbour Energy) for use of their Clair Field example. We thank TGS and partner AGS for the Utsira OBN regional data examples and Earth Science Analytics for the corresponding ML collaboration. We thank TGS and Directorate Generale de Hydrocarbures, Gabon for permission to show the Gabon Olumi Rouge data set. Finally, we thank TGS for permission to show the Declaration WAZ and Campos 3D NAZ data sets.

Data and materials availability

Data associated with this research are confidential and cannot be released.

Corresponding author: faqi.liu@tgs.com

References

He, Y., Y. He, H. Xing, Y. Huang, and B. Wang, 2021, Inversion-based imaging: FWI beyond velocity: 82nd Conference and Exhibition, EAGE, Extended Abstracts, https://doi.org/10.3997/2214-4609.202112698.

Huang, Y., J. Mao, C. Zeng, and J. Sheng, 2019, FWI salt model update trials with sparse nodes: 89th Annual International Meeting, SEG, Expanded Abstracts, 1255–1259, https://doi.org/10.1190/segam2019-3215169.1.

Jansen, S., A. C. Ramirez, D. Went, and B. Alaei, 2021, Benefits of using dense OBN for exploration: An example from Utsira using AI and machine learning: First Break, **39**, no. 10, 45–52, https://doi.org/10.3997/1365-2397.fb2021074.

Jiao, K., D. Sun, X. Cheng, and D. Vigh, 2015, Adjustive full waveform inversion: 85th Annual International Meeting, SEG, Expanded Abstracts, 1091–1095, https://doi.org/10.1190/segam2015-5901541.1.

Kalinicheva, T., M. Warner, and F. Mancini, 2020, Full-bandwidth FWI: 90th Annual International Meeting, SEG, Expanded Abstracts, 651–655, https://doi.org/10.1190/segam2020-3425522.1.

Luo, J., R.-S. Wu, and F. Gao, 2016, Time-domain full-waveform inversion using instantaneous phase with damping: 86th Annual International Meeting, SEG, Expanded Abstracts, 1472–1476, https://doi.org/10.1190/segam2016-13850128.1.

Luo, Y., Y. Ma, Y. Wu, H. Liu, and L. Cao, 2016, Full-traveltime inversion: Geophysics, **81**, no. 5, R261–R274, https://doi.org/10.1190/geo2015-0353.1.

Maharramov, M., A. I. Baumstein, Y. Tang, P. S. Routh, S. Lee, and S. K. Lazaratos, 2017, Time-domain broadband phase-only full-waveform inversion with implicit shaping: 87th Annual International Meeting, SEG, Expanded Abstracts, 1297–1301, https://doi.org/10.1190/segam2017-17744416.1.

Mao, J., J. Sheng, M. Hart, and T. Kim, 2016, High-resolution model building with multistage full-waveform inversion for narrow-azimuth acquisition data: The Leading Edge, **35**, no. 12, 1031–1036, https://doi.org/10.1190/tle35121031.1.

Mao, J., J. Sheng, and G. Hilburn, 2019, Phase only reflection full-waveform inversion for high resolution model update: 89th Annual International Meeting, SEG, Expanded Abstracts, 1305–1309, https://doi.org/10.1190/segam2019-3214447.1.

Mao, J., J. Sheng, Y. Huang, F. Hao, and F. Liu, 2020, Multi-channel dynamic matching full-waveform inversion: 90th Annual International Meeting, SEG, Expanded Abstracts, 666–670, https://doi.org/10.1190/segam2020-3427610.1.

Michell, S., X. Shen, A. Brenders, J. Dellinger, I. Ahmed, and K. Fu, 2017, Automatic velocity model building with complex salt: Can computers finally do an interpreter's job?: 87th Annual International Meeting, SEG, Expanded Abstracts, 5250–5254, https://doi.org/10.1190/segam2017-17778443.1.

Roende, H., D. Bate, J. Mao, Y. Huang, and D. Chaikin, 2020, New node acquisition design delivers unprecedented results with dynamic matching FWI — Case study from the Gulf of Mexico: First Break, **38**, no. 9, 73–78, https://doi.org/10.3997/1365-2397.fb2020068.

Shen, X., I. Ahmed, A. Brenders, J. Dellinger, J. Etgen, and S. Michell, 2017, Salt model building at Atlantis with full-waveform inversion: 87th Annual International Meeting, SEG, Expanded Abstracts, 1507–1511, https://doi.org/10.1190/segam2017-17738630.1.

Sheng, J., J. Mao, F. Liu, and M. Hart, 2020, A robust phase-only reflection full waveform inversion with multi-channel local correlation: 2020 Annual Conference and Exhibition Online, EAGE, Extended Abstracts, https://doi.org/10.3997/2214-4609.202012012.

Wang, B., Y. He, J. Mao, F. Liu, F. Hao, Y. Huang, M. Perz, and S. Michell, 2021, Inversion-based imaging: From LSRTM to FWI imaging: First Break, **39**, no. 12, 85–93, https://doi.org/10.3997/1365-2397.fb2021096.

Wang, P., Z. Zhang, J. Mei, F. Lin, and R. Huang, 2019, Full-waveform inversion for salt: A coming of age: The Leading Edge, **38**, no. 3, 204–213, https://doi.org/10.1190/tle38030204.1.

Warner, M., and L. Guasch, 2016, Adaptive waveform inversion: Theory: Geophysics, **81**, no. 6, R429–R445, https://doi.org/10.1190/geo2015-0387.1.

Zhang, Z., J. Mei, F. Lin, R. Huang, and P. Wang, 2018, Correcting for salt misinterpretation with full-waveform inversion: 88th Annual International Meeting, SEG, Expanded Abstracts, 1143–1147, https://doi.org/10.1190/segam2018-2997711.1.

Zhang, Z., Z. Wu, Z. Wei, J. Mei, R. Huang, and P. Wang, 2020, FWI imaging: Full-wavefield imaging through full-waveform inversion: 90th Annual International Meeting, SEG, Expanded Abstracts, 656–660, https://doi.org/10.1190/segam2020-3427858.1.